Electronic Supplementary Material (ESI) for Journal of Materials Chemistry A.
This journal is © The Royal Society of Chemistry 2023

# Supporting Information

## Rational nitrogen alloying in non-noble metal nickel–molybdenum nitride can mediate efficient and durable alkaline hydrogen evolution

Jia Yue Zhao,[a] Zhen Xin Lou,[a] Liang Yao Xue,[a] Yeliang Ding,[b] Xiaoxia Li,[b] Xuefeng Wu,[a] Yuanwei Liu,[a] Hai Yang Yuan, [a] Hai Feng Wang,[c] Peng Fei Liu,[a,*] Sheng Dai[d,*] and Hua Gui Yang[a,*]

[a] Key Laboratory for Ultrafine Materials of Ministry of Education, Shanghai Engineering Research Center of Hierarchical Nanomaterials, School of Materials Science and Engineering, East China University of Science and Technology, 130 Meilong Road, Shanghai 200237, China.
[b] China General Nuclear New Energy Holdings Co., Ltd., Beijing, 100071, China.
[c] Key Laboratory for Advanced Materials, School of Chemistry and Molecular Engineering, East China University of Science and Technology, 130 Meilong Road, Shanghai 200237, China.
[d] Key Laboratory for Advanced Materials and Feringa Nobel Prize Scientist Joint Research Center, Institute of Fine Chemicals, School of Chemistry and Molecular Engineering, East China University of Science and Technology, 130 Meilong Road, Shanghai 200237, China.

*E-mail address: hgyang@ecust.edu.cn (H. Yang); pfliu@ecust.edu.cn (P. Liu); shengdai@ecust.edu.cn (S. Dai)

## Experimental Section

**Materials:** Nickel foam (thickness: 1.6 mm, bulk density: 0.23 $g \cdot cm^{-3}$) was purchased from Heze Tianyu Technology Development Co., Ltd. Nickel nitrate hexahydrate ($Ni(NO_3)_2 \cdot 6H_2O$, 98.0%), nickel(II) chloride hexahydrate ($NiCl_2 \cdot 6H_2O$, 98%), ammonium molybdate tetrahydrate ($(NH_4)_6Mo_7O_{24} \cdot 4H_2O$, 99.0%), hydrochloric acid (HCl, 38.0%) and sulfuric acid ($H_2SO_4$, 98.0%) were purchased from Sinopharm Chemical Reagent Co., Ltd. Sodium molybdate ($Na_2MoO_4$, 99%) was purchased from Shanghai Lingfeng Chemical Reagent Co., Ltd. Ferric nitrate nonahydrate ($Fe(NO_3)_3 \cdot 9H_2O$, 99%) was purchased from Energy Chemical Co., Ltd. Chromium nitrate hexahydrate ($Cr(NO_3)_3 \cdot 6H_2O$, 99.95%) was purchased from Shanghai Macklin Biochemical Co., Ltd. Potassium hydroxide (KOH, 85.0%) was purchased from Yong Hua Chemical Co., Ltd. All chemicals were used as received without further purification and all water used for synthesis and analysis was purified to >18.2 MΩ cm by Millipore system.

**Pre-treatment of Ni foam:** Typically, a commercial nickel foam (geometric area of 1 $cm^2$ for performance evaluation) was sonicated with acetone and ethanol for 15 min, respectively. Then, the NF was put into a 3.0 M HCl solution for 15 min to clean the surface oxide layer. After that, the NF was washed with water and ethanol for several times and dried in a vacuum oven for the further use.

**Preparation of $NiMoO_4$/NF precursor:** In a typical synthesis procedure, 0.3491 g

$Ni(NO_3)_2 \cdot 6H_2O$ and 0.3709 g $(NH_4)_6Mo_7O_{24} \cdot 4H_2O$ were dissolved into 30 mL deionized water. The obtained solution with 3 pieces of above NF was then transferred into a 50 mL Teflon-lined stainless-steel autoclave reactor, remained at 150 °C for 6 h. After that, the reactor was immediately removed from the oven. When the reactor was cooled down to room temperature naturally, the resultant NFs were taken out and washed with deionized water for 3 times and with ethanol for 1 time, finally dried in vacuum at 60 °C

**Preparation of $Ni_2Mo_3N$/NF:** The above $NiMoO_4$/NF precursor samples were heated at 5 °C·min$^{-1}$ up to 700 °C for 2 h under $NH_3$ atmosphere (70 sccm) in a tube furnace, and then were cooled down to room temperature. After that, the synthesized electrocatalysts were ready for electrochemical tests. The loading amount of prepared catalyst is 17.19 mg cm$^{-2}$.

**Preparation of $NiMo_4N_5$/NF:** $NiMo_4N_5$/NF samples were prepared through the same method as $Ni_2Mo_3N$ except for the annealing temperature was changed to 600 °C. The loading amount of prepared catalyst is 16.00 mg cm$^{-2}$.

**Preparation of $NiMoO_4$/NF:** $NiMoO_4$/NF samples were prepared through the same method as $Ni_2Mo_3N$ except for the atmosphere during annealing was exchanged by Ar. The loading amount of prepared catalyst is 19.26 mg cm$^{-2}$.

**Preparation of NiMo alloy/NF:** In a typical synthesis procedure, 0.238 g $NiCl_2$ and 0.242 g $NaMoO_4$ were dissolved in 20 ml deionized water and the solution with pre-treated Ni foam was transferred into a 50 mL Teflon-lined stainless-steel autoclave reactor, remained at 160 °C for 6 h. After the reactor was cooled down to room temperature, the Ni foam was heated at 5 °C·min$^{-1}$ up to 550 °C for 2 h under $H_2$ atmosphere (40 sccm) in a tube furnace, and then was cooled down to room temperature. After that, the synthesized electrocatalyst was ready for electrochemical tests.

**Preparation of NiFeCr LDH/NF anode:** 20 mL of solution containing 0.27 g of $Fe(NO_3)_3 \cdot 9H_2O$, 0.872g of $Ni(NO_3)_2 \cdot 6H_2O$ and 0.133 g $Cr(NO_3)_3 \cdot 6H_2O$ was dropped into a three-necked flask containing 23 vol.% formamide solution (20 ml). Then, the three-necked flask was transferred to a low temperature reaction tank at 0 °C, and stirred with nitrogen for 10 minutes. A prepared 2.5 M NaOH solution was slowly added into the three-necked flask to maintain a pH of ~10. The reaction was completed within 15 minutes under a low-temperature nitrogen environment. The product was collected by centrifugation, washed repeatedly with deionized water and absolute ethyl alcohol, then kept in a wet state for subsequent use. For preparation of NiFeCr LDH /NF, 2ml of NiFeCr LDH suspension was dropped onto a 1.2 cm$^2$ Ni foam and the obtained NiFeCr LDH/NF was directly used as anode without any further process.

**Characterizations:** The morphologies of all samples were analyzed by scanning

electron microscopy (SEM, Hitachi S4800). The corresponding crystal structure was characterized by X-ray diffraction (XRD, D/max2550V). Scanning transmission electron microscopy (STEM) and transmission electron microscope (TEM) characterization was performed using ThermoFisher Talos F200X. High angle annular dark field (HAADF-STEM) images were recorded using a convergence semi angle of 11 mrad, and inner- and outer collection angles of 59 and 200 mrad, respectively. Energy dispersive X-ray spectroscopy (EDS) was carried out using 4 in-column Super-X detectors. The chemical states of the elements were examined by X-ray photoelectron spectroscopy (XPS, Kratos Axis Ultra DLD), and the energy corrections were calibrated by referencing the C 1s peak of adventitious carbon to 284.8 eV.

XAFS measurements at Ni and Mo K-edge in transmission mode were performed at the BL14W1 in Shanghai Synchrotron Radiation Facility. The electron beam energy was 3.5 GeV and the stored current was 230 mA (top-up). A 38-pole wiggler with the maximum magnetic field of 1.2 T inserted in the straight section of the storage ring was used. XAFS data were collected using a double-crystal Si (111) monochromator. The raw data analysis was performed using IFEFFIT software package according to the standard data analysis procedures. All samples performed in XAFS were prepared by collecting the catalyst powder from the electrode through sonicating.

**Electrochemical measurements:** The $NiMoO_4$/NF, $Ni_2Mo_3N$/NF, and blank NF were directly used as the working electrodes for electrochemical tests. All electrochemical studies were performed using an electrochemical station (CHI 660E) in a three-

electrode compartment with catalyst decorated Ni foam as the working electrode, an Ag/AgCl/3.5 M KCl electrode as the reference electrode and a graphite rod as the counter electrode. The Ag/AgCl/3.5 M KCl reference electrode was calibrated with respect to RHE. The calibration was performed in the high-purity $H_2$ saturated 1.0 M KOH electrolyte with Pt mesh as the working electrode and counter electrode. CVs were run at a scan rate of 1 mV $s^{-1}$, and the average of the two potentials at which the current crossed zero was taken to be the thermodynamic potential for the hydrogen electrode reactions (1.001 V in the 1.0 M KOH). The electrocatalytic activities towards HER were evaluated by polarization curves with a scan rate of 2 mV $s^{-1}$ in $H_2$-saturated 1.0 M KOH solution at ambient temperature. All potentials were referenced to reversible hydrogen electrode (RHE) by following calculations: $E_{RHE} = E_{Ag/AgCl} + 1.001$ V. All LSV curves were corrected with *iR* compensation (90%). For the stability tests, the $Ni_2Mo_3N$/NF was used as the working electrode directly and the chronopotentiometric curve was conducted at the constant *j* of -10 mA $cm^{-2}$ with 90% *iR* compensation. To obtain the EIS spectra for HER reactions, a frequency range of $10^5$ Hz to 0.01 Hz was set up at the $\eta$ of -100 mV. ECSA measurements were collected by CV from $C_{dl}$ and ECSA can be calculated as below: $ECSA = C_{dl\text{-}catalyst} / C_s$. The CV tests were acquired with a range of 0.08 - 0.18 V vs. RHE at different scan rates (10, 20, 30, 40, and 50 mV·$s^{-1}$).

**DFT calculations:** All the spin-polarized calculations were performed using the Vienna Ab-initio Simulation Package (VASP) package[1-3]. The exchange-correlation

functional was described by the Perdew-Burke-Ernzerhof (PBE) functional[4] within the generalized gradient approximation (GGA)[5]. The project-augmented wave (PAW) method[6] was employed to treat core electrons, and the cutoff energy of plane-wave basis was set to 450 eV. The Broyden method was used for geometric optimization, and as the forces on all relaxed atoms were less than 0.05 eV/Å, the optimizations were stopped. The (221) surface was selected as the object, on which a vacuum space of 15 Å was added on the surface. During the optimization, the bottom two atomic layers kept frozen, and others are completely relaxed. A corresponding 1×1×1 k-point mesh was used. The transition states (TSs) were searched by the constrained optimization scheme.[7, 8]

**Gibbs free energy of dissociation:** The dissociation tendency of nitride is to become the corresponding pure metal and $NH_3$, which can be defined as:

$$A_aB_bN_{c\,(s)} + 3c(H^+ + e^-) \rightarrow aA_{\,(s)} + bB_{\,(s)} + cNH_{3\,(g)} \quad (1)$$

For the sake of simplification, each metal is considered to form a non-interfering elemental metal[9]. The total free energy of the dissociation reaction ($\Delta E_d$) was calculated using the computational hydrogen electrode (CHE). In this approach, the chemical potentials of a proton-electron pair ($H^+/e^-$) and an $H_2$ molecule are equilibrated at 0 V (vs. the reversible hydrogen electrode, RHE) at all pH values[10, 11]:

$$\Delta E_d = \Delta E + neU \quad (2)$$

Where $\Delta E$ is the change of energy in the decomposition reaction (1), and the additional term ($neU$) is intended to correct for some of the effects of the electrochemical environment (n is the number of electrons transferred).

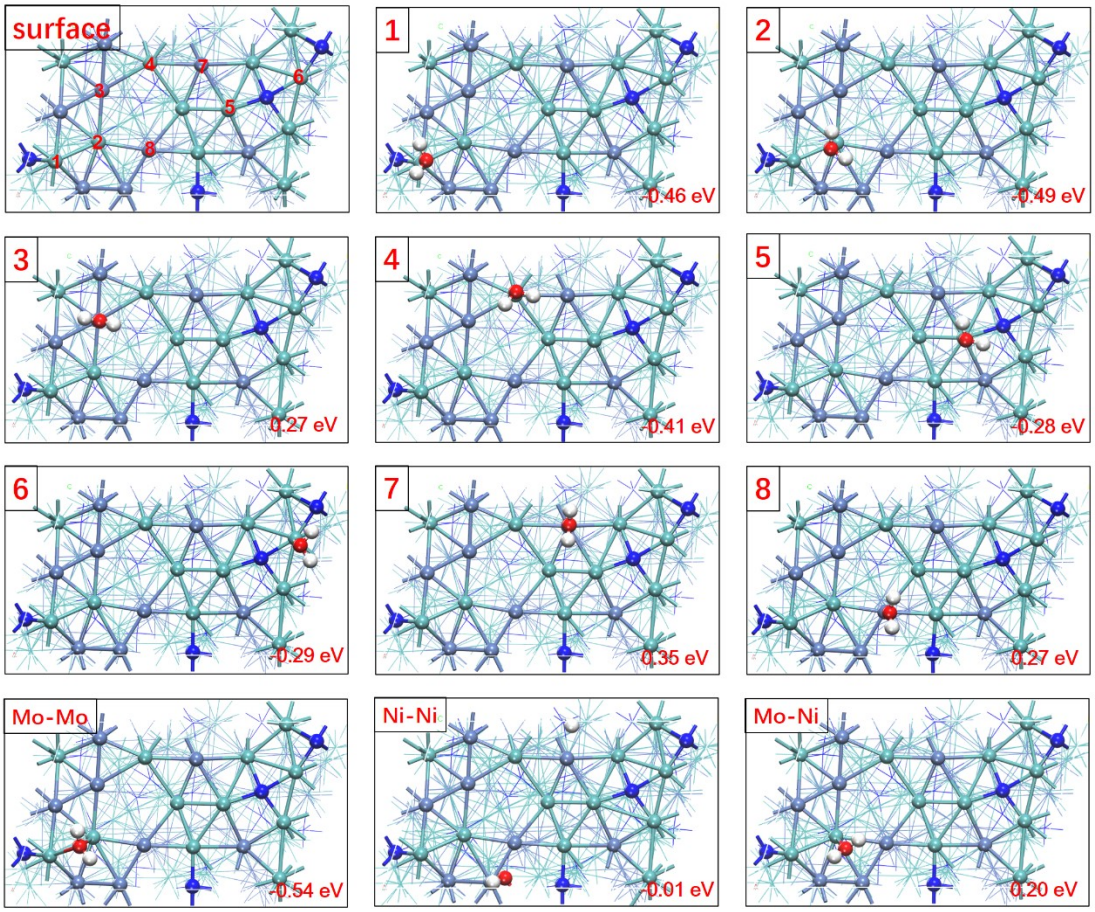


**Fig. S1.** Adsorption configurations of $H_2O$ on different sites of $Ni_2Mo_3N$ (221) surface.

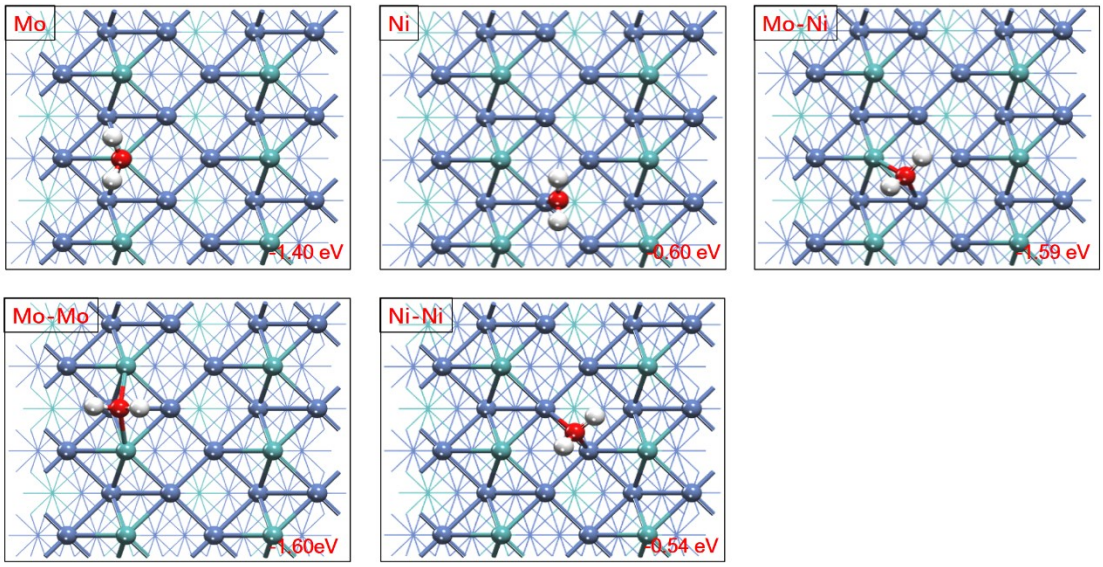


**Fig. S2.** Adsorption configurations of $H_2O$ on different sites of $Ni_4Mo$ (100) surface.

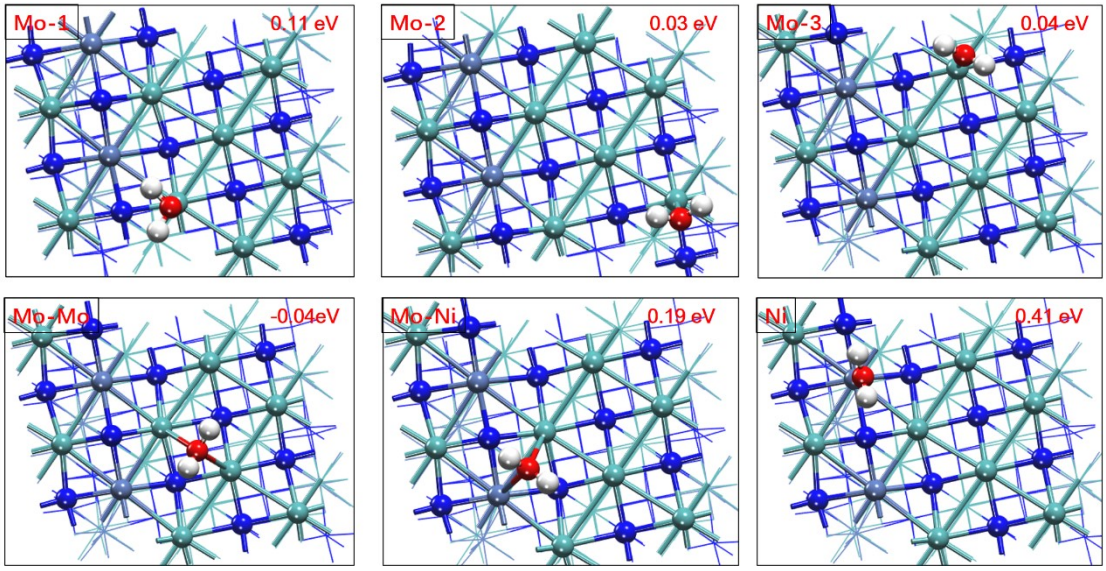


**Fig. S3.** Adsorption configurations of $H_2O$ on different sites of $NiMo_4N_5$ (111) surface.

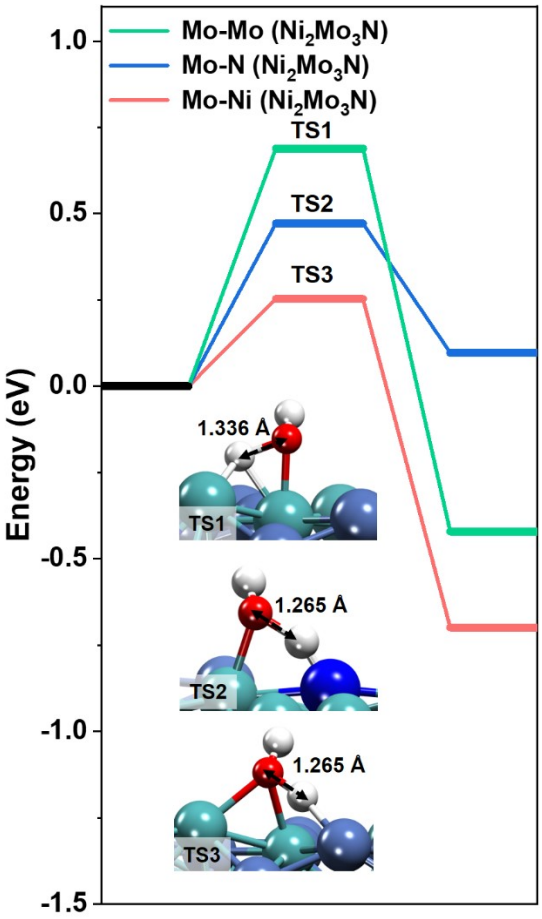


**Fig. S4.** Energy profiles of $H_2O$ adsorbed on Mo site of $Ni_2Mo_3N$ dissociating assisted by Mo (green) Ni (red) and lattice N (blue) sites, and the corresponding transition states are shown by TS1 ~ TS3, respectively.

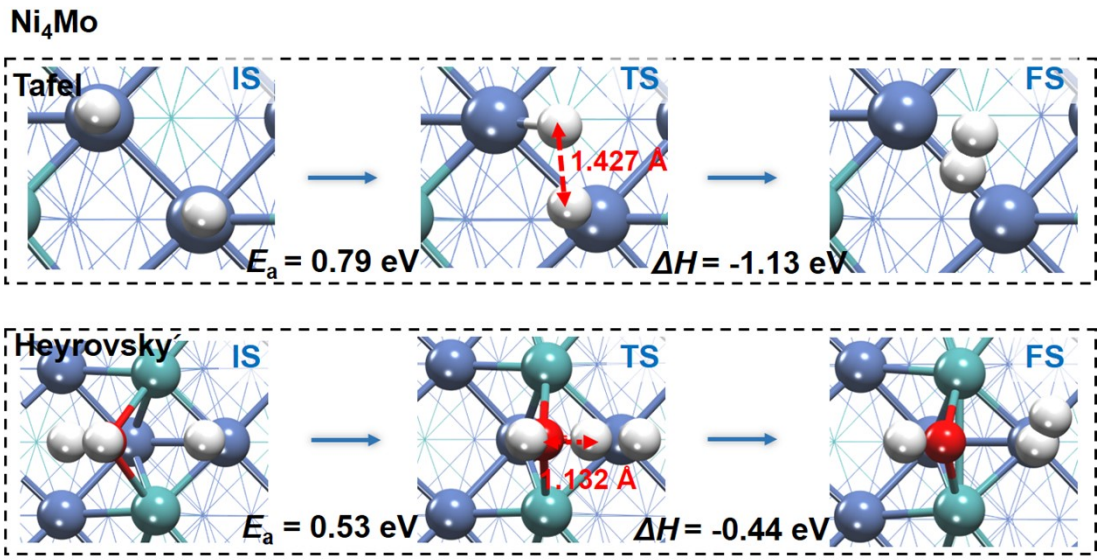


**Fig. S5.** The Schematic diagrams of the $H_2$ generation for $Ni_4Mo$, including the Tafel step (*H + *H → $H_2$ + 2*) and Heyrovsky step ($H_2O$ + *H + $e^-$ → $H_2$ + $OH^-$ + *). The structure from left to right is the initial state (IS), transition state (TS) and final state (FS), respectively.

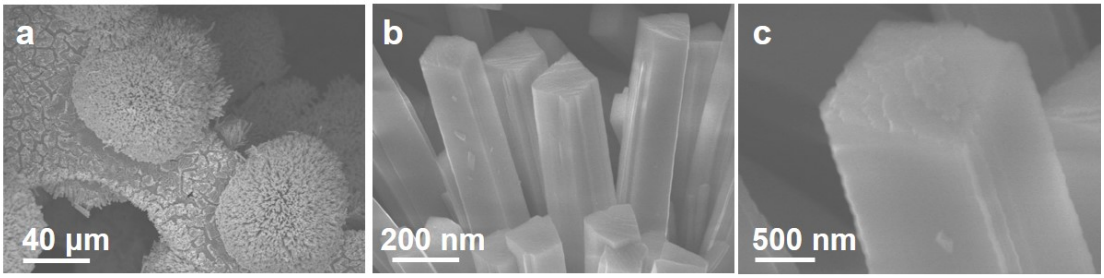


**Fig. S6.** (a-c) SEM images of $NiMoO_4$ precursor at different magnifications, showing the rod-like morphology. (b, c) Magnified SEM images in (a) of rod-like $NiMoO_4 \cdot xH_2O$ precursor.

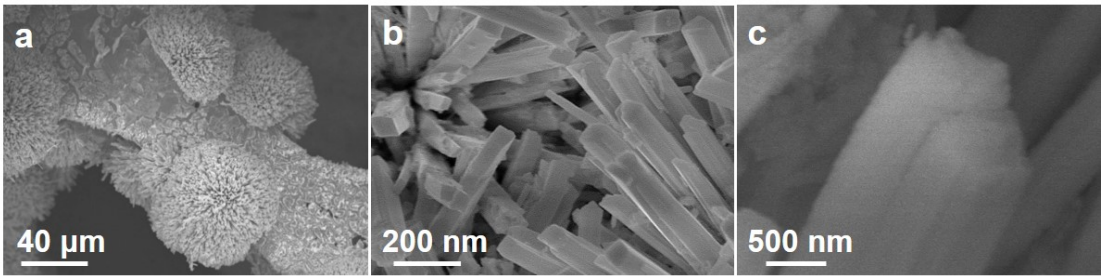


**Fig. S7.** (a-c) SEM images of $NiMoO_4$ precursor after annealed in Ar atmosphere under 700 °C at different magnifications. (b, c) Magnified SEM images in (a) of $NiMoO_4$ after treatment in Ar, showing no obvious morphology changes after heat treatment.

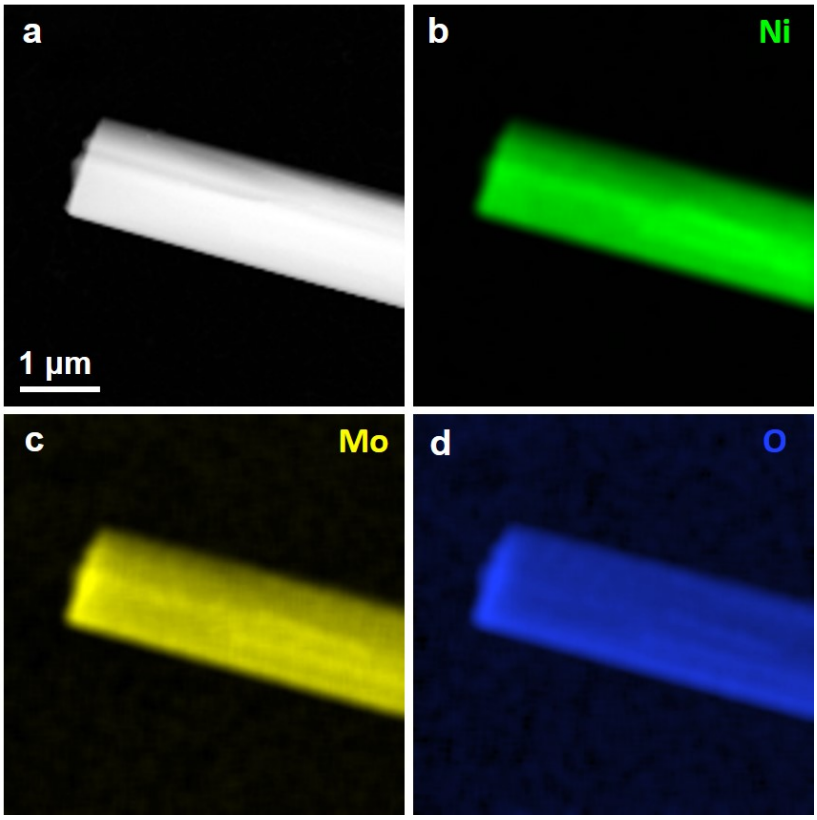


**Fig. S8.** (a) HAADF STEM image of $NiMoO_4$ precursor, indicating the smooth surface. (b-d) The corresponding EDS elemental maps of Ni, Mo, and O, respectively in $NiMoO_4 \cdot xH_2O$, illustrating the rod-like morphology and homogenous distribution of Ni, Mo, and O elements.

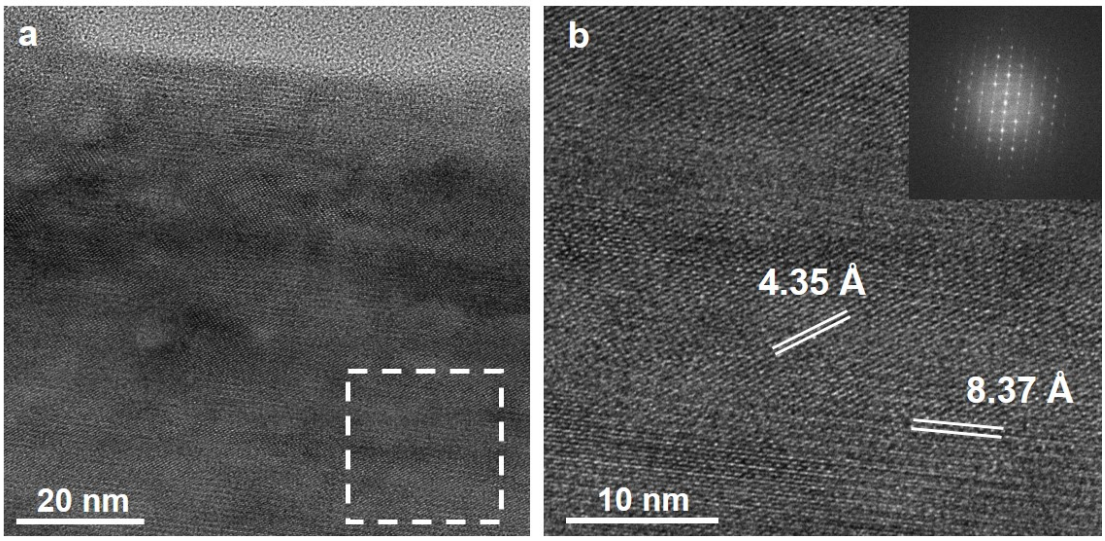


**Fig. S9.** (a) HRTEM image of $NiMoO_4 \cdot xH_2O$ and (b) the magnified image of marked region and corresponding FFT pattern. The measured interplanar spacing fits well with $NiMoO_4 \cdot xH_2O$, while the FFT pattern demonstrates its high crystalline.

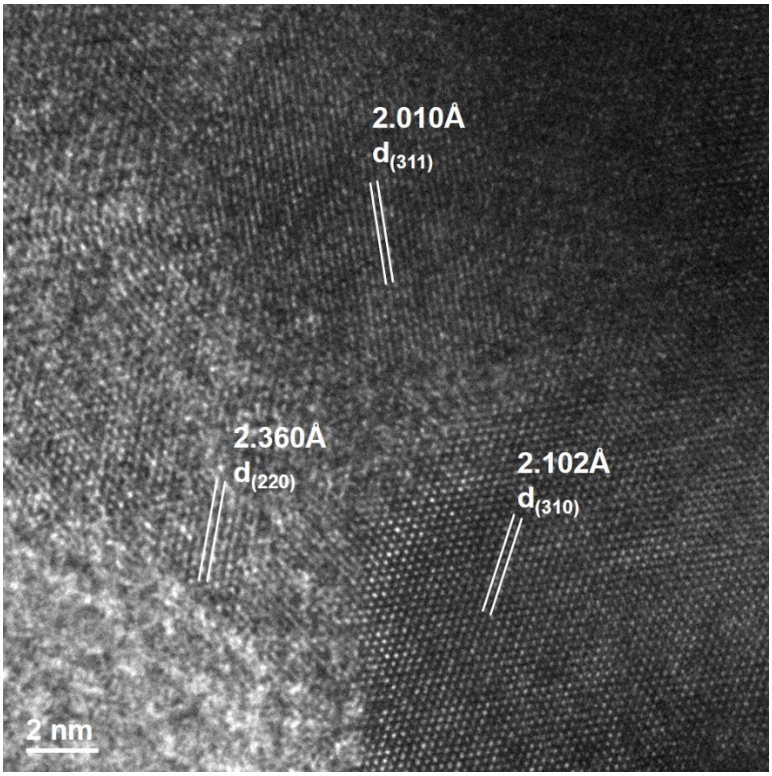


**Fig. S10.** HRTEM image of $Ni_2Mo_3N$ powder. The measured interplanar spacing demonstrates the formation of $Ni_2Mo_3N$.

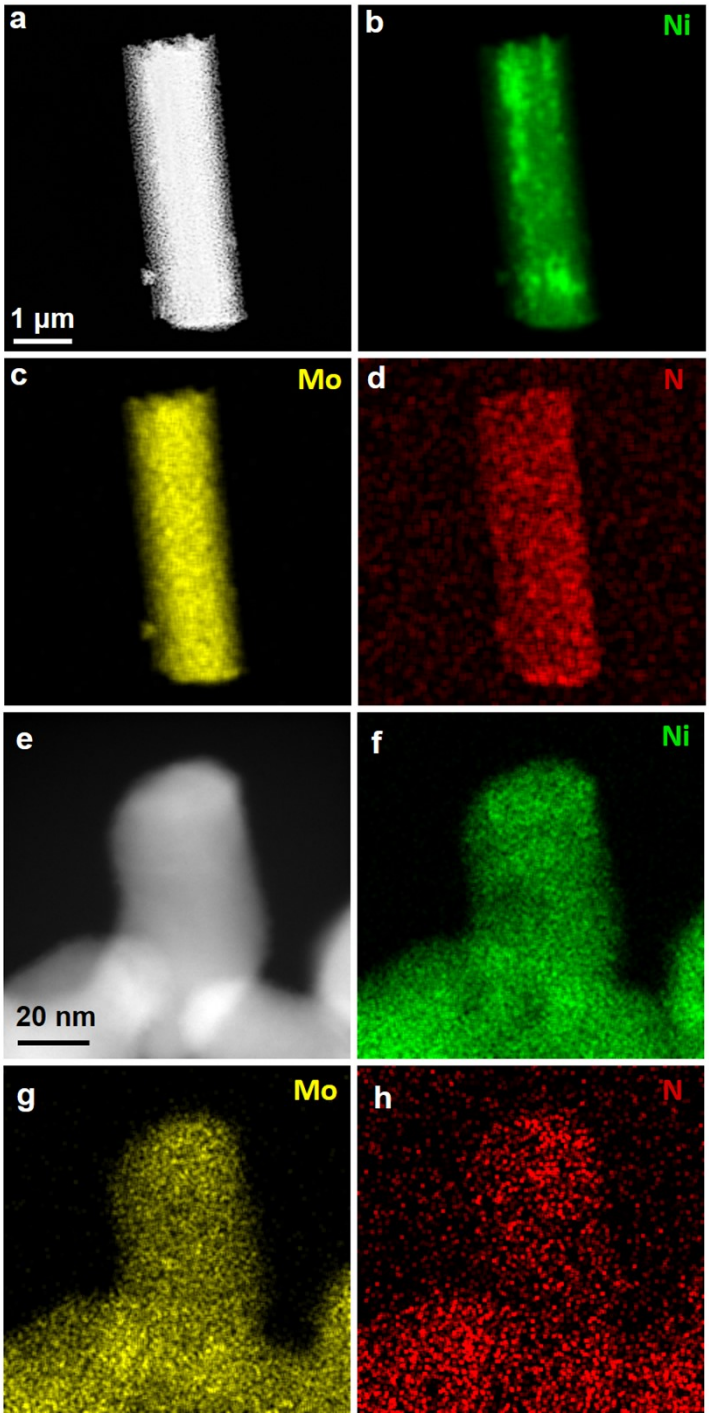


**Fig. S11.** (a) HAADF STEM image of $Ni_2Mo_3N$ and (b-d) corresponding EDS elemental maps of Ni, Mo, and N, respectively, showing the rod-like nanoporous morphology. (e) The enlarged HAADF STEM image of $Ni_2Mo_3N$ and corresponding EDS elemental maps of Ni, Mo, and N, respectively, indicating the uniform distribution of Ni, Mo, and N elements.

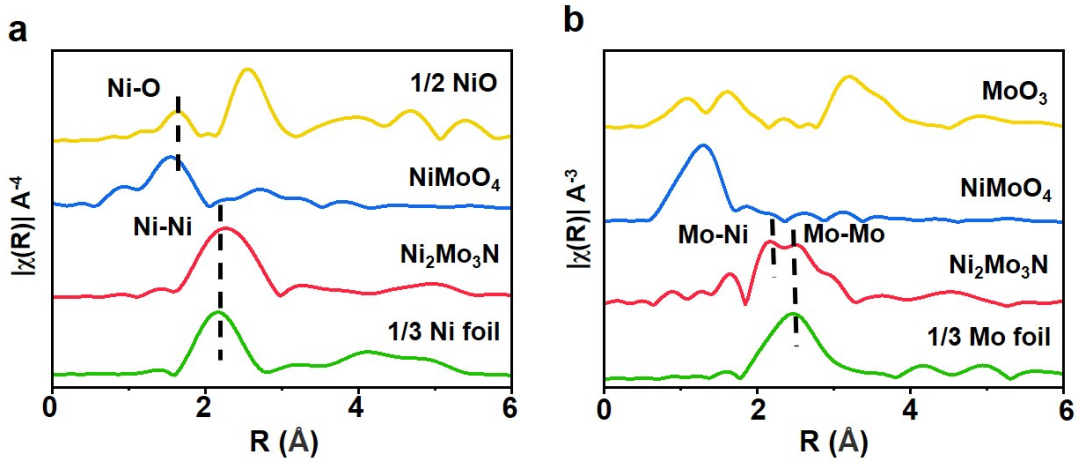


**Fig. S12.** (a) Ni K-edge EXAFS spectra of $Ni_2Mo_3N$ in R space and reference samples, (b) Mo K-edge EXAFS spectra of $Ni_2Mo_3N$ in R space and reference samples.

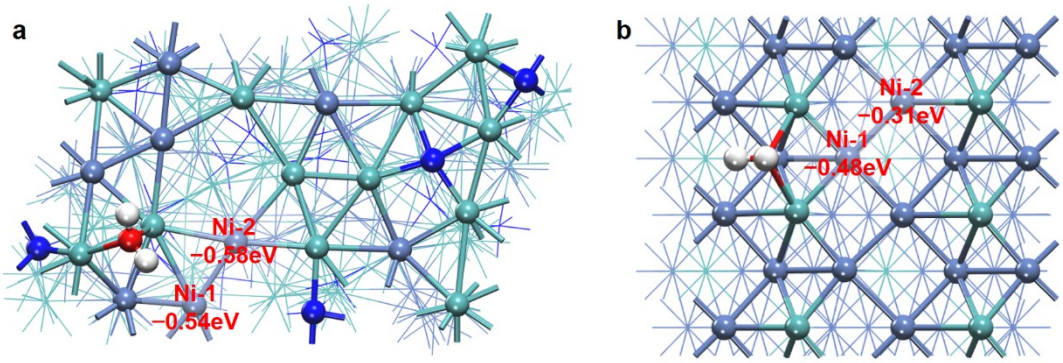


**Fig. S13.** Bader charge analysis of the Ni sites (H receptor) in (a) $Ni_2Mo_3N$ and (b) $Ni_4Mo$ with $H_2O$ adsorbed.

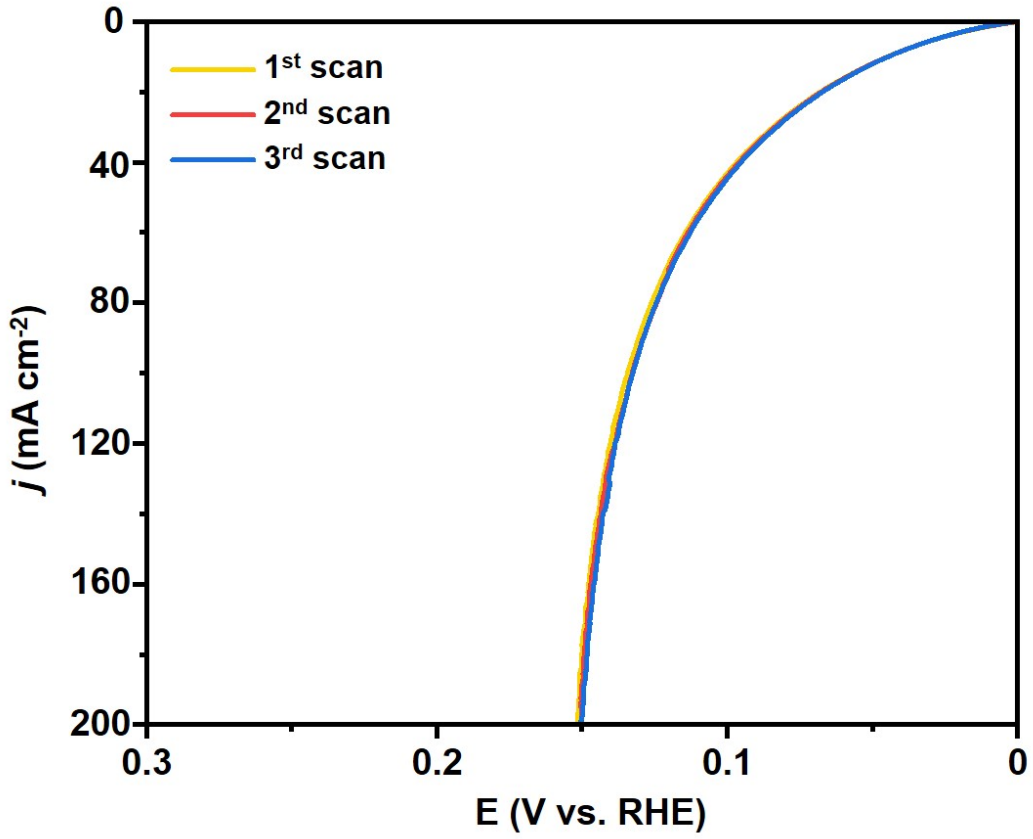


**Fig. S14.** LSV curves of $Ni_2Mo_3N$/NF in 1.0 M KOH collected from 3 independent tests.

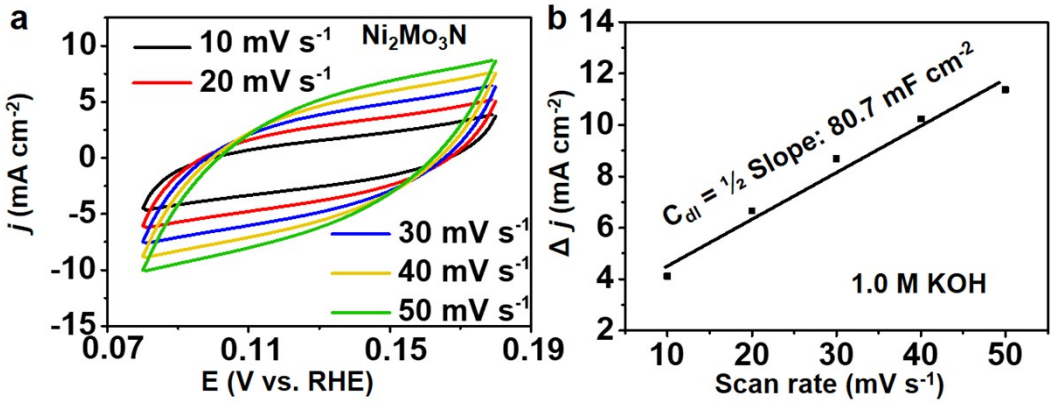


**Fig. S15.** (a) Cyclic voltammograms of $Ni_2Mo_3N$ for HER at different scan rates (from 10 to 50 mV $s^{-1}$ with an increment of 10 mV $s^{-1}$) in 1.0 M KOH. (b) Scan rates dependence of the current densities ($\Delta j = j_a - j_c$) for $Ni_2Mo_3N$/NF.

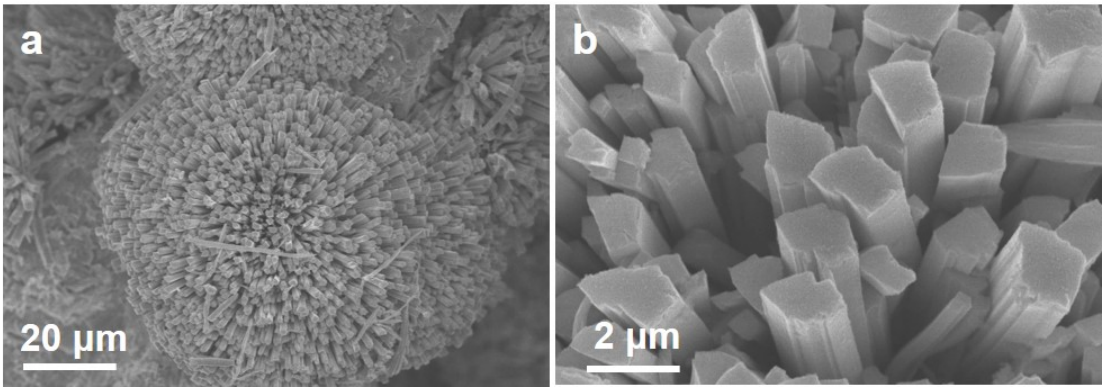


**Fig. S16.** SEM image of $Ni_2Mo_3N$ after HER test in the alkaline solution, indicating the structure stability for maintaining the rod-like morphology.

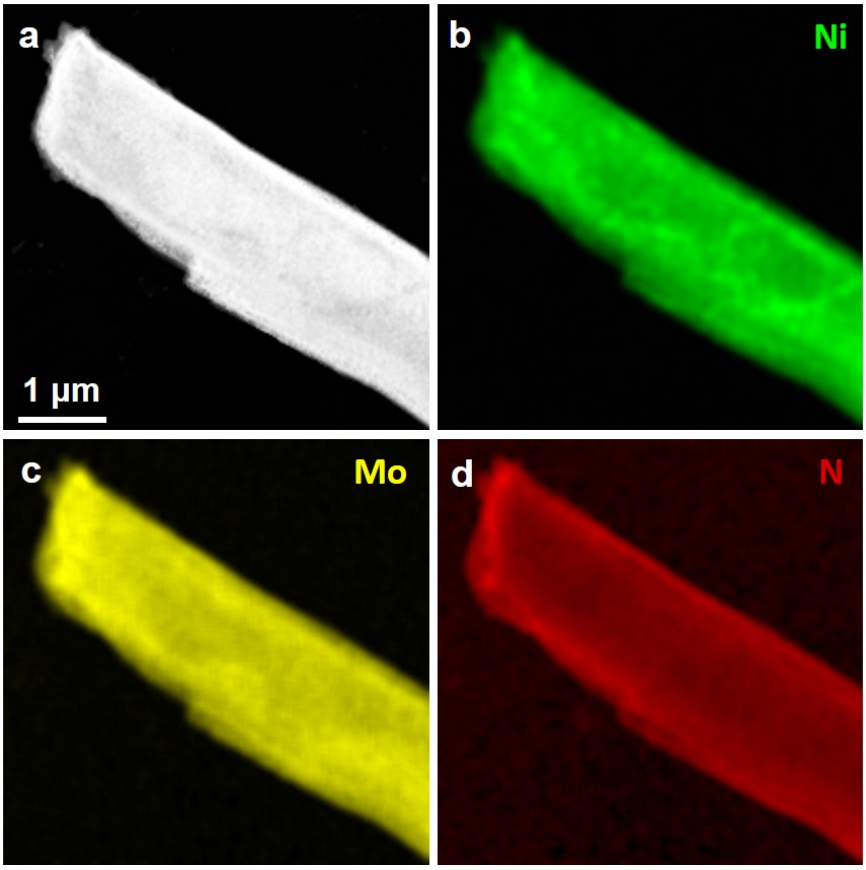


**Fig. S17.** (a) HAADF STEM image of $Ni_2Mo_3N$ after HER test in the alkaline solution and (b-d) the corresponding EDS elemental maps of Ni, Mo, and N, respectively, illustrating the maintaining of nanoporous structure and homogenous distribution of Ni, Mo, and N elements.

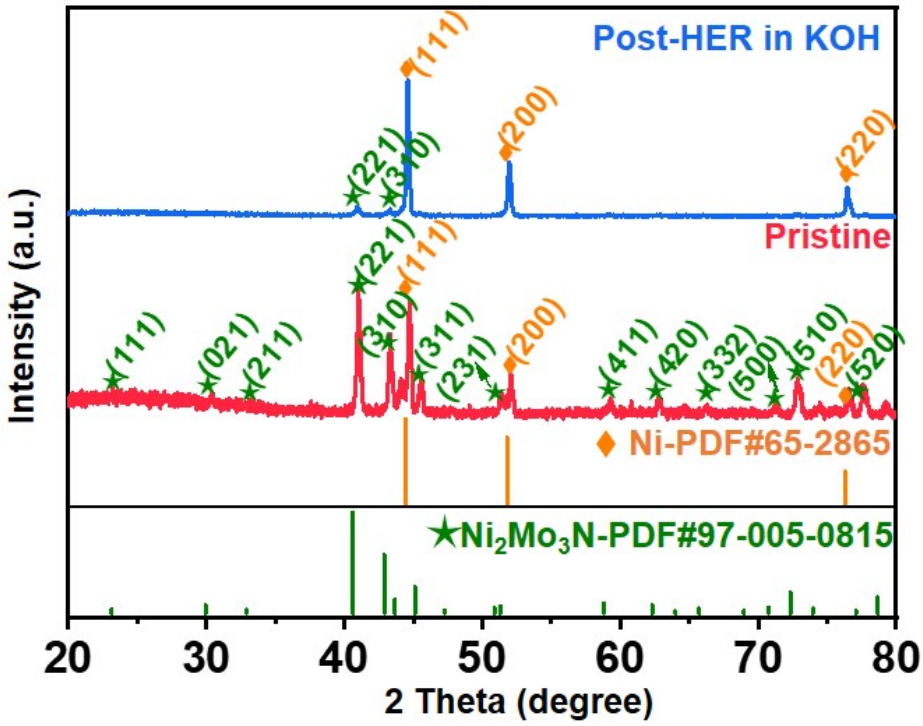


**Fig. S18.** XRD patterns of $Ni_2Mo_3N$/NF before and after HER test in 1.0 M KOH solution, showing the poor crystallinity after alkaline HER test. The characteristic diffraction peaks of (221) and (310) of $Ni_2Mo_3N$ could still be observed.

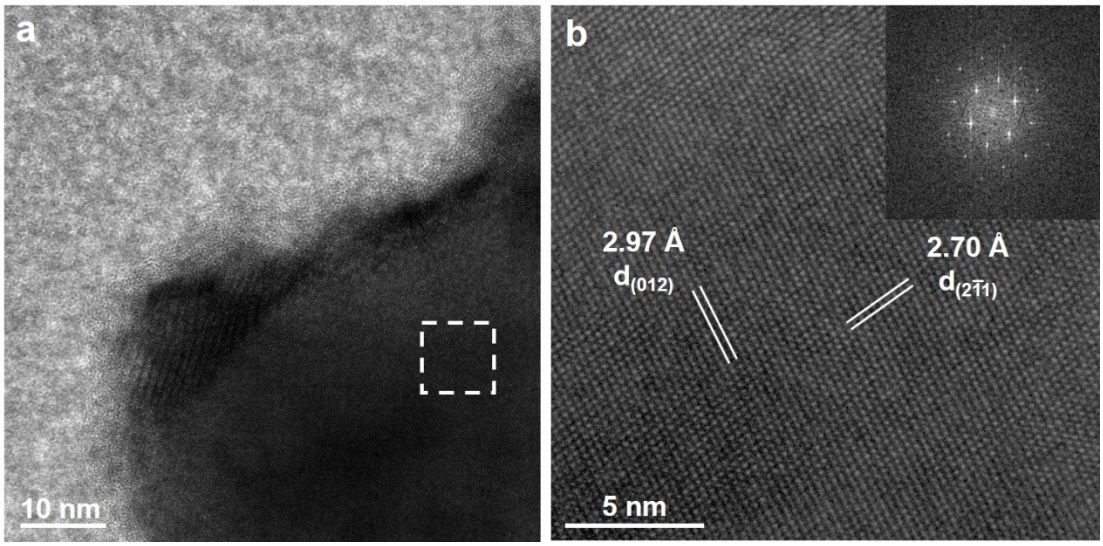


**Fig. S19.** (a) HRTEM image of $Ni_2Mo_3N$ collected after HER test in 1.0 M KOH and (b) the magnified image of marked region and corresponding FFT pattern, which suggests the existence of crystallized $Ni_2Mo_3N$, indicating that the $Ni_2Mo_3N$ exhibits a stable crystal structure after HER test.

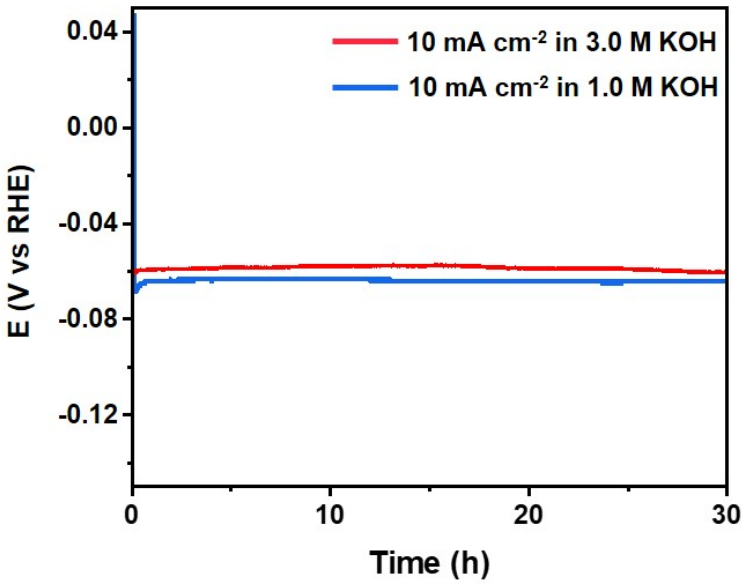


**Figure S20.** Chronopotentiometric curve of $Ni_2Mo_3N$ electrode at the applied current density of 10 mA $cm^{-2}$ for continuous HER in 3.0 M and 1.0 M KOH.

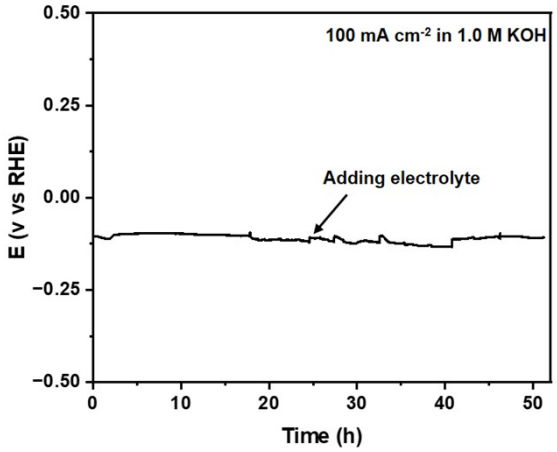


**Figure S21.** Chronopotentiometric curve of $Ni_2Mo_3N$ electrode at the applied current density of 100 mA $cm^{-2}$ in 1.0 M KOH at ambient temperature for continuous HER.

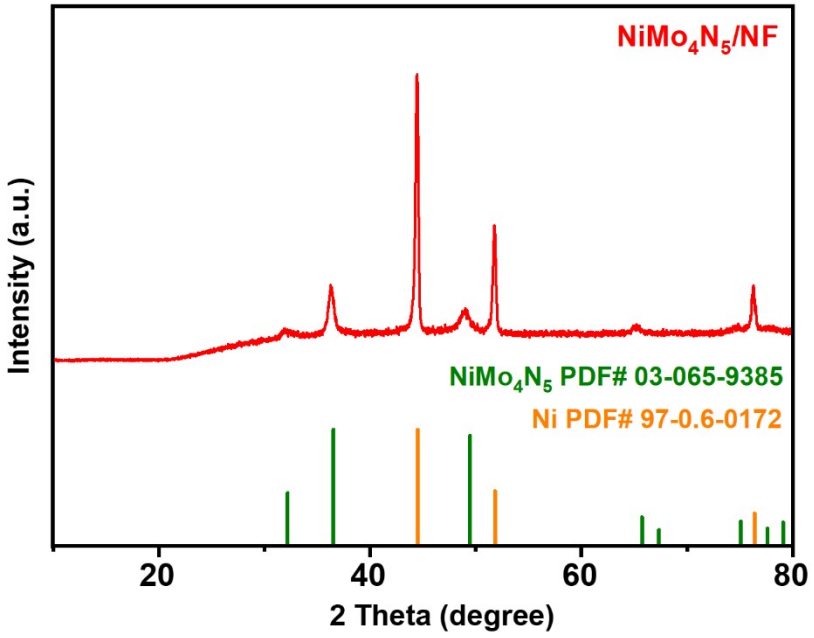


**Fig. S22.** XRD patterns of $NiMo_4N_5$/NF, showing the corresponding diffraction peaks as standard $NiMo_4N_5$.

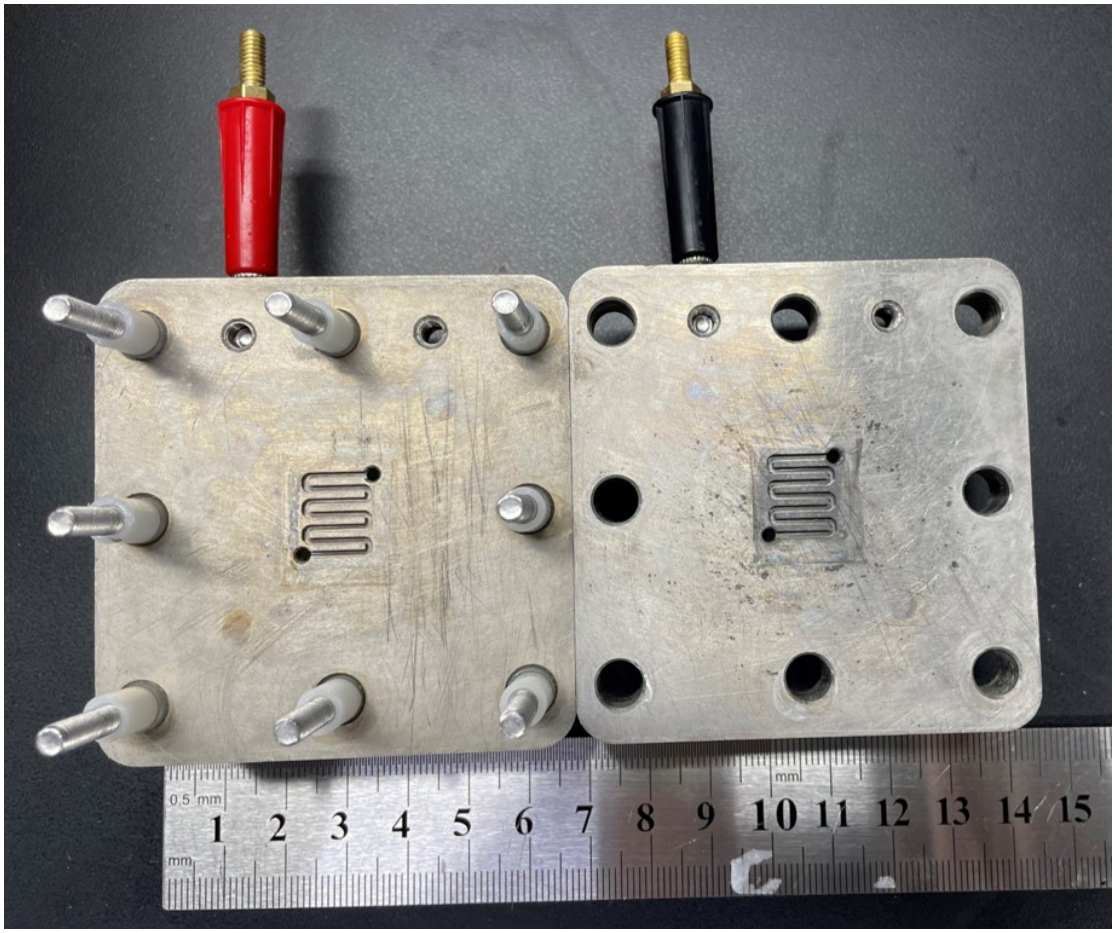


**Fig. S23.** Digital photo of the applied MEA for alkaline water splitting with the flow field area of 1.2 $cm^2$.

**Table S1.** Structural parameters extracted from the Ni K-edge EXAFS fitting

| Sample | Path | *N* | *R*(Å) | $\sigma^2$($10^{-3}$ Å$^2$) | $\Delta E_0$(eV) | *R*-factor |
|---|---|---|---|---|---|---|
| | Ni-N | 1.0 | 2.14±0.03 | 9.5 | | |
| $Ni_2Mo_3N$ | Ni-Ni | 6.6±0.9 | 2.51±0.01 | 11.5±1.9 | 5.0±1.2 | 0.001 |
| | Ni-Mo | 5.7±0.6 | 2.73±0.01 | 10.7±1.7 | | |

Notes: N is the coordination number; *R* is interatomic distance (the bond length between central atoms and surrounding coordination atoms); $\sigma^2$ is Debye-Waller factor (a measure of thermal and static disorder in absorber-scatterer distances); $\Delta E_0$ is edge-energy shift (the difference between the zero kinetic energy value of the sample and that of the theoretical model). *R*-factor is used to value the goodness of the fitting.

**Table S2.** Structural parameters extracted from the Mo K-edge EXAFS fitting

| Sample | Path | $N$ | $R$(Å) | $\sigma^2$($10^{-3}$ Å$^2$) | $\Delta E_0$(eV) | $R$-factor |
|---|---|---|---|---|---|---|
| | Mo-N | 1.7±0.4 | 2.08±0.08 | 3.6±2.9 | | |
| $Ni_2Mo_3N$ | Mo-Ni | 5.8±0.9 | 2.76±0.04 | 11.2±1.5 | -1.5±5.3 | 0.013 |
| | Mo-Mo | 3.5±2.5 | 2.81±0.04 | 3.3±2.8 | | |

**References**

(1) G. Kresse, J. Furthmiiller, *Comput. Mater. Sci.*, 1996, **6**, 15.
(2) G. Kresse, J. Hafner, *Phys. Rev. B*, 1993, **47**, 558.
(3) G. Kresse, J. Hafner, *Phys. Rev. B*, 1994, **49**, 14251.
(4) G. Kresse, J. Furthmüller, *Phys. Rev. B*, 1996, **54**, 11169.
(5) P. Perdew, John, K. Burke, M. Ernzerhof, *Phys. Rev. Lett.*, 1996, **77**, 3865.
(6) G. Kresse, D. Joubert, *Phys. Rev. B*, 1999, **59**, 1758.
(7) H. Y. Yuan, N. N. Sun, J. F. Chen, J. M. Jin, H. F. Wang, P. J. Hu, *ACS Catal.*, 2018, **8**, 9269.
(8) J. M. Jin, J. F. Chen, H. F. Wang, P. J. Hu, *Chin. Chem. Lett.*, 2019, **30**, 618.
(9) Y. Abghoui, A. L. Garden, V. F. Hlynsson, S. Björgvinsdóttir, H. Ólafsdóttir, E. Skúlason, *Phys. Chem. Chem. Phys.*, 2015, **17**, 4909-4918.
(10) J. K. Nørskov, J. Rossmeisl, A. Logadottir, L. Lindqvist, J. R. Kitchin, T. Bligaard, H. Jónsson, *J. Phys. Chem. B*, 2004, **108**, 17886.
(11) A. Garza, A. Bell, M. Head-Gordon, *ACS Catal.*, 2018, **8**, 1490.